

Magnetization of $\text{SrCu}_2(\text{BO}_3)_2$ in ultrahigh magnetic fields up to 118 T: *supplemental material*

Y. H. Matsuda,¹ N. Abe,¹ S. Takeyama,¹ H. Kageyama,² P. Corboz,³
A. Honecker,^{4,5} S. R. Manmana,⁴ G. R. Foltin,⁶ K. P. Schmidt,⁶ and F. Mila⁷

¹*Institute for Solid State Physics, University of Tokyo, Kashiwa, Chiba 277-8581, Japan*

²*Graduate School of Engineering, Kyoto University, Nishikyoku, Kyoto 615-8510, Japan*

³*Theoretische Physik, ETH Zürich, CH-8093 Zürich, Switzerland*

⁴*Institut für Theoretische Physik, Georg-August-Universität Göttingen, D-37077 Göttingen, Germany*

⁵*Fakultät für Mathematik und Informatik, Georg-August-Universität Göttingen, D-37073 Göttingen, Germany*

⁶*Lehrstuhl für Theoretische Physik I, Otto-Hahn-Straße 4, TU Dortmund, 44221 Dortmund, Germany*

⁷*Institute of Theoretical Physics, Ecole Polytechnique Fédérale de Lausanne (EPFL), 1015 Lausanne, Switzerland*

(Dated: August 19, 2013)

This supplemental material is organized as follows: In Secs. **I-III** details on the experimental techniques for the generation of ultrahigh magnetic fields over 100 T and the magnetization measurements are given. In Sec. **IV** we provide an overview of the numerical methods used in our study of the Shastry-Sutherland model. In Sec. **V** we present the spin structures of the phases mentioned in the main text. Finally, in Sec. **VI** we compare the different numerical results for the extent of the 1/3 and 1/2 plateau phases, and discuss magnetization curves obtained for different values of J'/J in comparison with the experimental data.

I. SINGLE-TURN COIL TECHNIQUE

The generation of a strong magnetic field exceeding 100 T is technically very difficult because of the huge Maxwell force. A great deal of effort has been done to extend the field range; a record of a magnetic field of 100.75 T was recently obtained in nondestructive manner [1]. However, it is widely recognized that a magnetic field far above 100 T is only generated in a destructive manner, i.e., by destroying the magnet. The electromagnetic flux compression (EMFC) method allows us to generate high fields over 700 T [2, 3]. However, since everything inside the magnet including the sample are completely destroyed in the EMFC experiment, substantial effort is required to repeat the experiment.

The single-turn coil (STC) technique is useful for high magnetic field experiments up to 200 T. Although the magnet (single-turned coil) is broken in the field generation process, the sample and the cryostat inside the coil survives with almost no damage [4]. The coil for the STC technique is lightweight and rather small as shown in Fig. 1. Hence the experiment is much easier than EMFC.

The vertical type STC in the Institute for Solid State Physics, University of Tokyo [5], was utilized in the present study. The coil is vertically set to the electrode so that a liquid-helium bath cryostat is inserted into the coil bore. The photo of the set-up of the coil and the cryostat is shown in Fig. 2. A capacitor bank is used as the power source; the full electrical capacitance is 263.5 μF and the maximum charging voltage is 40 kV. The typical waveform of the generated magnetic field using a single-turn coil with 14 mm diameter is shown in Fig. 1 in the main text.

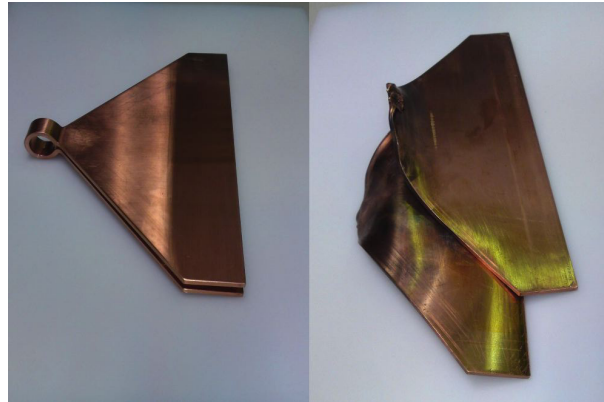


FIG. 1. A single-turn coil before the experiment (left) and after the experiment (right). The inner diameter of the coil in this picture is 14 mm.

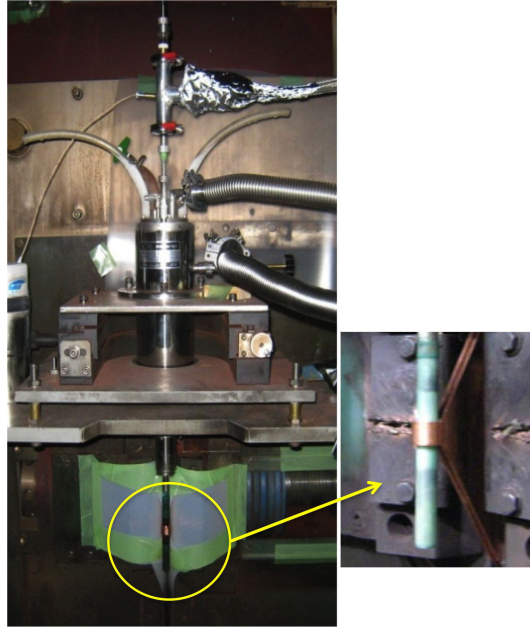


FIG. 2. The vertical type single-turn coil apparatus; a helium bath cryostat is installed. A single-turn coil with 14 mm diameter is inserted.

II. A HELIUM BATH CRYOSTAT SPECIALLY DESIGNED FOR THE VERTICAL STC

The duration time of the magnetic field generated by the STC is $6 - 9 \mu\text{s}$. Such a high speed pulsed magnetic field with an intense peak value larger than 100 T gives rise to a large induction current in metals located near by the coil. For instance, a metal tube inside the coil would be strongly deformed and might cause an implosion due to the strong electromagnetic force between the induction current and the magnetic field. Therefore a helium bath cryostat with the tail section made of a fiber-reinforced glass epoxy (so-called FRP or G10) was specially designed [6]. The schematic diagram of the cryostat is shown in Fig. 3. The sample is immersed in liquid helium. A low temperature down to 2 K is reached by evacuation of helium vapor.

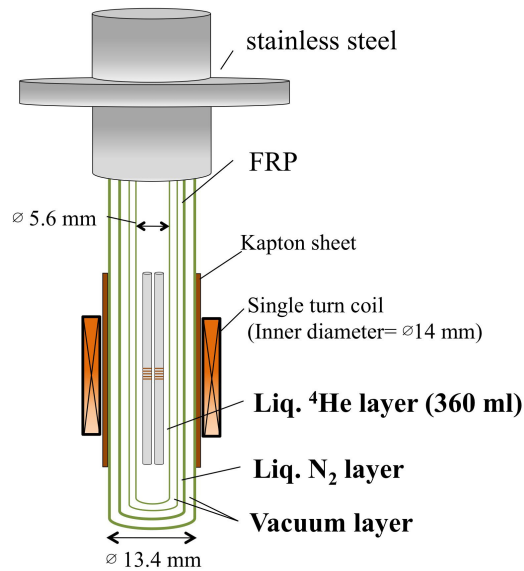


FIG. 3. Schematic diagram of the cryostat specially designed for the vertical STC.

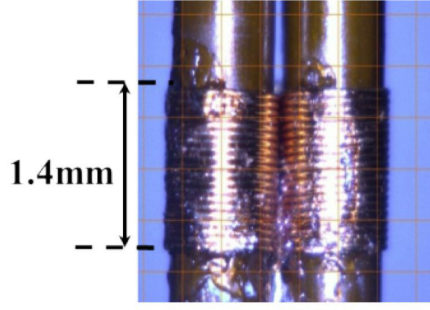


FIG. 4. Photograph of the pickup coil for the magnetization measurement .

III. MAGNETIZATION MEASUREMENT USING THE STC

The magnetization measurement was performed using a pair of pickup coils as shown in Fig. 4. It is wound 20 turns around a polyimide tube (with an outer diameter of 1.12 mm) by a copper wire (with a diameter of 60 μm) for each coil. The coils are series-connected and have opposite polarization so that the induction voltage by an applied magnetic field is canceled. When a sample is inserted into the right pickup coil (R-coil) while the left coil (L-coil) remains empty, the signal induced in the R-coil (V_R) and that in the L-coil (V_L) are described as

$$\begin{aligned} V_R &= S_{\text{eff}}^A \mu_0 \frac{dH}{dt} + S_{\text{eff}}^A \frac{dM}{dt} \\ V_L &= -S_{\text{eff}}^B \mu_0 \frac{dH}{dt}. \end{aligned} \quad (1)$$

Here, S_{eff}^A and S_{eff}^B are the effective area of the pickup coils (including the number of turns), respectively, and μ_0 is the magnetic permeability of the vacuum. H denotes the applied magnetic field. The obtained signal in the experiment is

$$V_1 = V_R + V_L = (S_{\text{eff}}^A - S_{\text{eff}}^B) \left(\mu_0 \frac{dH}{dt} \right) + S_{\text{eff}}^A \frac{dM}{dt}. \quad (2)$$

A great deal of effort is done to make the coils such that $S_{\text{eff}}^A \sim S_{\text{eff}}^B$ and the condition that $(S_{\text{eff}}^A - S_{\text{eff}}^B)/S_{\text{eff}}^A \sim 10^{-4}$ is required for precise measurements. This is because the induction voltage for each coil ($S_{\text{eff}}^{A(B)} \mu_0 \frac{dH}{dt}$) can become as high as 1000 V.

The first term of eq. (2) is the background noise owing to the imperfect compensation between the R- and L-coils. This is further canceled by repeating the measurement with the condition that the sample position is exchanged from the R-coil to L-coil. The signal obtained in the second measurement is

$$V_2 = V_R + V_L = (S_{\text{eff}}^A - S_{\text{eff}}^B) \left(\mu_0 \frac{dH}{dt} \right) - S_{\text{eff}}^B \frac{dM}{dt}. \quad (3)$$

Finally, the signal that is proportional to the magnetization is obtained as follows,

$$V = V_1 - V_2 = (S_{\text{eff}}^A + S_{\text{eff}}^B) \frac{dM}{dt} \sim 2S_{\text{eff}}^A \frac{dM}{dt}. \quad (4)$$

The dM/dt signal plotted in Fig. 1 in the main text was deduced from eq. (4).

IV. NUMERICAL METHODS

A. Exact diagonalization

Exact diagonalization (ED) using the Lanczos method is a versatile tool for studying low-dimensional quantum models (see, e.g., Ref. 7). ED has also been widely applied to the $S = 1/2$ Shastry-Sutherland model. Nevertheless, to the best of our knowledge, there are only two publications where exact diagonalization results on Shastry-Sutherland lattices with more than 32 spins have been reported [8, 9]: Ref. 8 has presented a magnetization curve at $J'/J = 0.6$ for $N = 32$ and 36 and Ref. 9 has studied the phase diagram in a magnetic field using exact diagonalization for $N = 32$ and 36, but only for $J'/J \leq 0.5$.

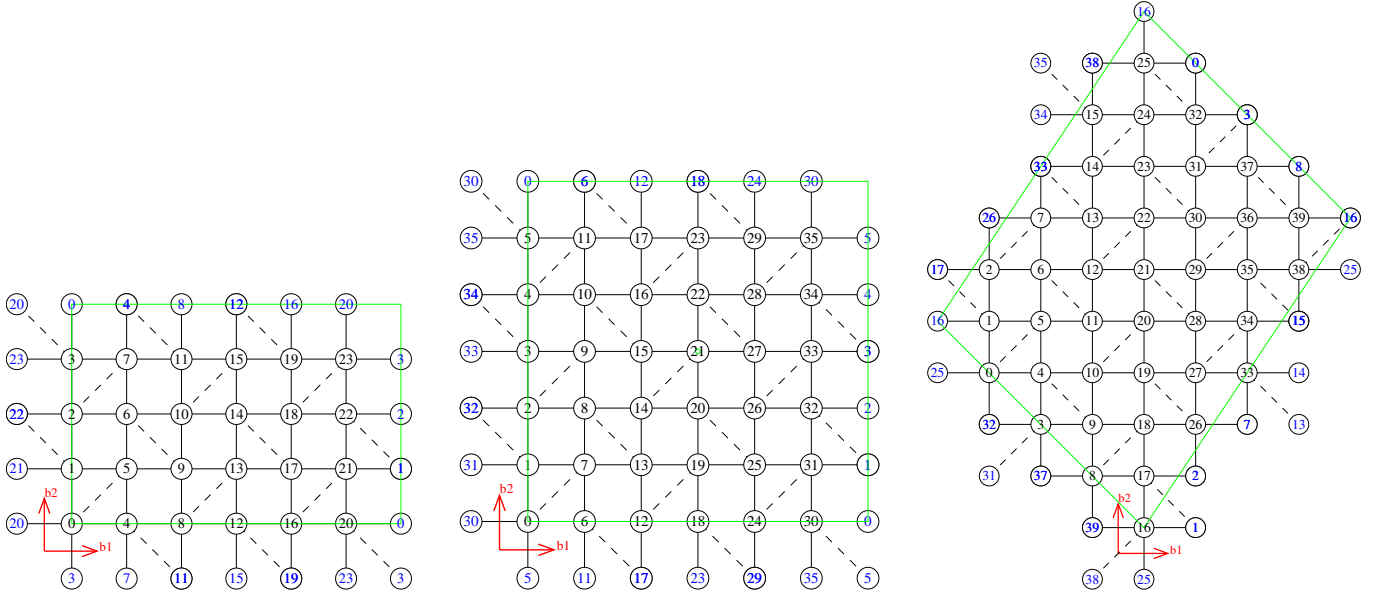


FIG. 5. From left to right: The $N = 24, 36$, and 40 sites Shastry-Sutherland lattices used for ED in the present work. The $6 \times 6 = 36$ site lattice is also used for the DMRG simulations. The larger systems used with DMRG are obtained starting from this lattice and adding an even number of columns and rows, respectively.

The present computations have been performed with SPINPACK [10]. We have employed periodic boundary conditions in order to minimize finite-size effects and to permit using translational symmetries. In addition, we have used point group symmetries and conservation of total S^z . Still, Hilbert space dimensions remain comparably large due to the big unit cell of the Shastry-Sutherland lattice which contains 4 spins. Therefore, we are restricted to lattices with $N \lesssim 40$ spins even if we use MPI parallelization on up to 1536 cores.

Due to the limited system sizes, attention must be paid to finite-size effects when interpreting ED data. Firstly, one should keep in mind that the $T = 0$ magnetization curve for a finite lattice consists of at most $N/2$ steps (for $M \geq 0$) and only magnetizations $M/M_S = 2n/N$ with n integer and $|n| \leq N/2$ are realized. Additional finite-size effects will arise if the structure of the ground state is incommensurate with the lattice under consideration. The lattices for which we present data are shown in Fig. 5.

B. Density matrix renormalization group

The density matrix renormalization group method (DMRG) and related matrix product state (MPS) approaches are standard tools for treating (quasi-)one-dimensional systems, in particular also spin systems in magnetic fields [11, 12], and recently it has been applied successfully to two-dimensional systems [13–16]. Here, we attempt to characterize the phase diagram of the 2D Shastry-Sutherland model at all values of the magnetization, which is a far more challenging task than analyzing the ground state at $M = 0$ only. Since we are tackling the problem in a combination of methods, using the DMRG we focus solely on the magnetization curve at a few values of J'/J in order to support the results obtained by iPEPS and to the degree possible extend the analysis of finite clusters performed by ED to larger system sizes. This is achieved by computing the ground state energy for systems with periodic boundary conditions (PBC) in both spatial directions and cluster sizes of $6 \times 6, 8 \times 6, 8 \times 8, 10 \times 8, 10 \times 10$, and 12×10 spins. Due to the PBC, boundary effects on the energy are avoided. Typically, we obtain the energies per site at all values of the magnetization with an accuracy of the order of $5 \cdot 10^{-3}$ or better (in typical ground state calculations in one-dimensional systems, an accuracy in the energy per site of the order of 10^{-9} can be achieved). However, it is difficult to guarantee that the DMRG does not get stuck in excited states, as comparison with ED data for clusters with 6×6 sites at larger values of J'/J than the ones discussed here has shown. In principle, this uncertainty can lead to artifacts in the magnetization curve which, however, should not appear in a systematic way throughout the data obtained for different system sizes. Therefore, if we identify a signature for a plateau in different system sizes, we interpret the finding in that way that the DMRG in these cases converged within the aforementioned accuracy to the correct state.

Usually, converging the energy at this low accuracy leads to wave functions which can be qualitatively wrong, so that local

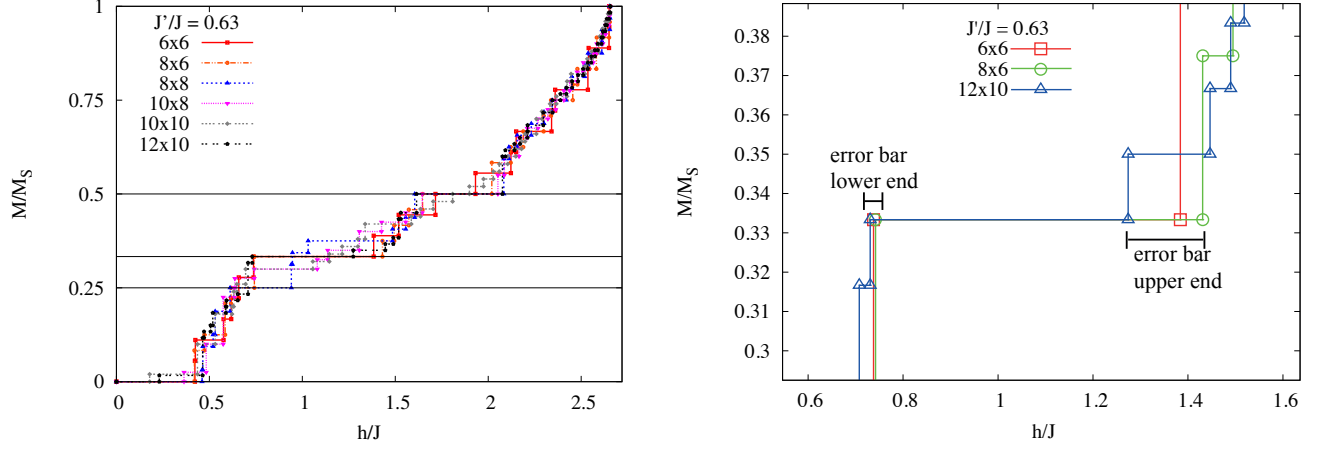


FIG. 6. (a) ‘Raw’ DMRG results for the magnetization curves obtained for the different system sizes at $J'/J = 0.63$. (b) Zoom into the region containing the $1/3$ plateau with data for the system sizes allowing for a plateau at this value of M . We estimate the error bars for the positions of the plateaus by considering the values for the different system sizes; as can be seen, for the lower end, a rather small error bar is obtained, while at the upper end the error bar is significantly larger, possibly indicating the presence of a shallowly growing magnetization curve following this plateau.

observables and correlation functions can show the wrong behavior. However, due to the $U(1)$ symmetry of the system, for computing the magnetization curves we only need the energies of the ground states in all sectors of S_{total}^z , which is only a single number per run and also the most accurate observable obtained by the DMRG, since it is a variational method. Thus, despite the difficulties to reach better convergence, we can apply PBC in both spatial dimensions, which is the most challenging scenario for the DMRG. Together with the estimate of the error bars presented in this section, this allows us to obtain the magnetization curve with a good precision, so that we can compare to results obtained by the other approaches.

For the results presented here, typically we perform 40 sweeps and keep up to $m = 2000$ density matrix eigenstates. The resulting discarded weight is typically of the order of 10^{-4} or smaller. Despite the large number of sweeps and states kept, the energy can still change in the course of the last DMRG sweeps, so that in estimating the error bar additional caution needs to be taken. We obtain the magnetization curves shown in Fig. 6(a). (The results for systems with more than 10×8 spins are obtained from comparing runs with different DMRG parameters and by taking the lowest achieved energies for a given value of S_{total}^z). The sizes and positions of the plateaus at $1/4$, $1/3$, and $1/2$ agree well with the iPEPS results. As can be seen, the data seems to collapse to a continuous magnetization curve in the high-field regions, but the accuracy is not high enough to exclude further plateaus at $2/3$ and $3/4$, and possibly additional values of M . In the low field region, the lower the magnetization and the larger the system size, the more difficult it is to reach convergence, so that DMRG data below $M = 1/4$ needs to be considered with care; also, for the larger system sizes, it is difficult to obtain a unifying picture from the results between $M = 1/4$ and $M = 1/2$.

In Fig. 6(b) we show at the example of the $M = 1/3$ plateau how we estimate the error bars in the extensions of the plateaus by comparing the results for the critical fields for the different system sizes. In Fig. 10(b) below we compare the resulting endpoints of the plateaus to the ones obtained by iPEPS for $J'/J = 0.63$ (see next section). Good agreement is obtained; however, at the upper end of the $1/3$ plateau the error bars are large. This might indicate a shallow increase of the magnetization at the end of this plateau, which would make it difficult to obtain the end point with a high accuracy.

C. Infinite projected entangled-pair states

An infinite projected entangled-pair state (iPEPS) is an efficient variational ansatz for a wave function in two dimensions in the thermodynamic limit [17–19]. It can be seen as a two-dimensional extension of a matrix product state (MPS) – the underlying variational ansatz of the density-matrix renormalization group method. An iPEPS on the square lattice consists of a unit cell of 5th order tensors which is periodically repeated on the lattice [20]. Each tensor has one physical index, which runs over the d basis states of a lattice site, and four auxiliary indices with a certain bond dimension D which connect to the four nearest neighboring tensors. The number of variational parameters per tensor is dD^4 , thus the larger D the (potentially) more accurate the ansatz.

As a local basis we take the four basis states of a dimer, i.e., we simulate a square lattice model where each lattice site corresponds to one of the orthogonal dimers. For details on the simulations and iPEPS we refer to Ref. 21 where a similar

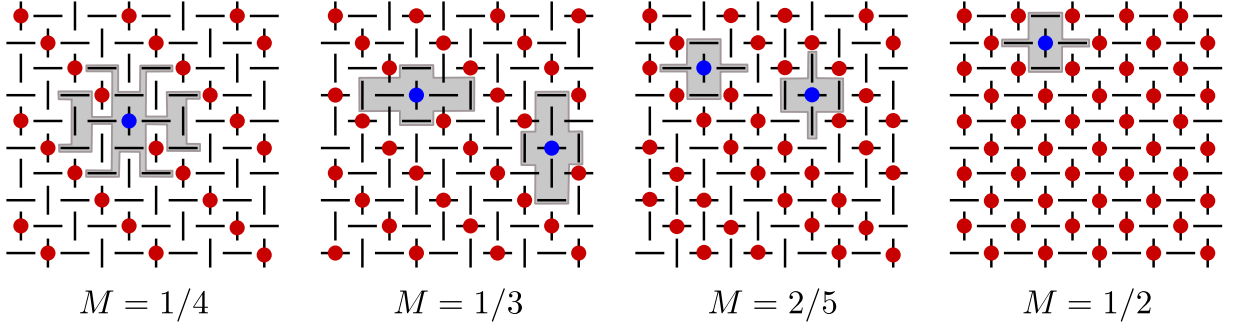


FIG. 7. Illustration of the plateau structures considered by series expansion. Red dots denote triplets t^1 while empty dimers correspond to the presence of singlets s . The gray areas Γ_i^M contain for each plateau all repulsive interactions involving the blue triplet on dimer i which have to be put in the unperturbed Hamiltonian \hat{H}_0 .

simulation setup was used for the Shastry-Sutherland model without an external magnetic field. The results presented are obtained with the so-called simple update in iPEPS, which gives a reasonably good estimate for the energy, and we checked several simulations with the more accurate (but computationally more expensive) full update (see Ref. 19 for details).

By using different unit cell sizes an iPEPS can represent different translational symmetry broken states. To find the ground state for each value of H and J'/J we have performed simulations with various rectangular unit cell sizes up to 18×18 to determine which cell yields the lowest variational energy. We have run simulations up to $D = 6$ for the supersolid phases (up to $D = 8$ for $J'/J = 0.63$), and up to $D = 8$ for the states within a plateau where we exploited the (unbroken) $U(1)$ symmetry [22].

To obtain an estimate of the energy in the infinite D limit we linearly extrapolate the finite D data in $1/D$, which gives a value E_{extrap} . Empirically we find that the energy converges faster than linearly in $1/D$, thus E_{extrap} is likely to underestimate the true energy. As an estimate we therefore take the mean between this value and the value at the largest D , i.e., $E_{D=\infty} = (E_{D_{\text{max}}} + E_{\text{extrap}})/2$, and a rough estimate of the error bar is provided by half of the difference between these two values, i.e., $\Delta = (E_{D_{\text{max}}} - E_{\text{extrap}})/2$.

We determine the phase transition between two phases by determining the intersection point of the energies $E_{D=\infty}$ of the two adjacent phases, as e.g. done in Refs. 19, 21, and 23. To obtain an estimate of the error bar on the phase transition we determine the intersection of the energies, where we take a lower (underestimated) value for the energy in one of the phases, $E_{\text{low}} = E_{D=\infty} - \Delta/2$, and a higher (overestimated) value of the energy in the other phase $E_{\text{high}} = E_{D=\infty} + \Delta/2$. This will lead to a shift of the phase boundary towards the second phase. Similarly, we take E_{high} for the first phase and intersect it with E_{low} of the second phase to obtain the other part of the error bar.

For a transition between a plateau phase and an adjacent supersolid phase we find that the phase boundary moves towards the plateau phase with increasing D , i.e., at finite values of D the size of a plateau is overestimated. Therefore, we can obtain an upper bound of the phase boundary by taking the intersection of the energies of the two phases at a fixed $D = 6$.

The transition between the $1/3$ plateau state and the $1/3$ supersolid phase is found to be of second order. In order to have a lower bound on the phase boundary we linearly extrapolate the magnetization $M(H)$ and intersect it with $M = 1/3$. (We checked for $J'/J = 0.63$ and full update iPEPS simulations that this extrapolation yields a lower bound on the phase boundary). We use this estimate of the lower bound also for the transition between the $2/5$ plateau and $2/5$ supersolid, and the $1/2$ plateau and the $1/2$ supersolid phase.

D. Series expansion

In the following we shortly explain how we have implemented high-order series expansions for the magnetization plateaux at $M = 1/2$, $M = 2/5$, $M = 1/3$, and $M = 1/4$. For each plateau we calculated the ground-state energy per dimer. Additionally, the one-particle gap for the plateau structures at $M = 1/2$ and $M = 1/3$ is determined.

We aim at setting up a high-order series expansion for the most relevant magnetization plateaux at $M = 1/2$, $M = 2/5$, $M = 1/3$, and $M = 1/4$. The idea is to *deform* the Shastry-Sutherland model such that one can define an unperturbed Hamiltonian \hat{H}_0 which has as a unique ground state a product state of singlets s and triplets t^1 with the desired magnetization M and plateau structure as illustrated in Fig. 7.

Physically, this is achieved in two steps. First, we add a magnetic field of strength J to \hat{H}_0 . As a consequence, on an isolated dimer one has two degenerate low-energy states, the singlet s and the triplet t^1 , while the other two states t^0 and t^{-1} cost a finite

energy. Second, one adds repulsive interactions between triplets t^1 to \hat{H}_0 and by subtracting the same kind of interactions in the perturbation \hat{V} introducing the perturbative parameter $x \in [0, 1]$. The Shastry-Sutherland model is then recovered for $x = 1$. To be specific, we define

$$\hat{H}_M = J \left(\hat{H}_J + \hat{H}_h + \lambda \hat{H}_M \right) + x \left(J' \hat{H}_{J'} - \lambda J \hat{H}_M \right) + (h - J) \hat{H}_h, \quad (5)$$

$$= \hat{H}_0 + x \hat{V} + (h - J) \hat{H}_h, \quad (6)$$

where $\hat{H}_M = \sum_i \hat{n}_i \sum_{j \in \Gamma_i^M} \hat{n}_j$ with $\hat{n}_i = \hat{t}_{1,i}^\dagger \hat{t}_{1,i}$. Here Γ_i^M corresponds to a specific collection of dimers around dimer i which can differ for each plateau structure. The Γ_i^M are illustrated in Fig. 7 as gray areas. The parameter λ is a parameter one can choose freely which might result in an improved convergence of the series. Here we have chosen $\lambda = 1$ for all plateaux except $M = 1/2$ where a $\lambda < 1$ gives better results.

The series expansion is done in the perturbative parameter x . We used Loewdin's projector method [24] to calculate the ground-state energy per dimer ϵ_M in the thermodynamic limit. We have obtained order 9 for ϵ_M with $M = 1/2$, $M = 2/5$, $M = 1/3$ and order 8 for $\epsilon_{1/4}$. Additionally, we used Takahashi's degenerate perturbation theory [25, 26] to calculate the one-particle gap Δ_M for $M = 1/2$ and $M = 1/3$. Here we have calculated order 9 for $M = 1/2$ and order 7 for $M = 1/3$ [27]. In all cases one has to fix the ratio J'/J and one has to perform the extrapolation in x up to $x = 1$.

One can deduce two kinds of information from the different series expansions: i) Location of first-order phase transitions between two different plateaux. To this end one defines $f_M(h) = \epsilon_M + (h - J)M$. A first-order phase transition between the plateaux with magnetizations M and M' then takes place at h_{1st} for which $f_M(h_{1st}) = f_{M'}(h_{1st})$. ii) The breakdown of a plateau with magnetization M by a second-order phase transition can be located by the help of the one-particle gap Δ_M . If one finds $\Delta_M < h_{1st}$ for a fixed ratio J'/J , then one expects a second-order phase transition at $h = \Delta_M + J$ to a supersolid phase with the same kind of crystalline order. Note that the series expansion is not sensitive to first-order phase transitions to other plateaux with different M .

V. OVERVIEW OF PHASES

In Fig. 8 we present the spin structures of the different phases mentioned in the main text. These phases have been obtained with iPEPS using different rectangular unit cells, as explained in Sec. IV C.

We note that slightly above the $1/2$ plateau state there is also a competing $2/5$ supersolid phase. However, we have found that the $1/3$ supersolid phase is energetically slightly lower.

VI. COMPARISON BETWEEN NUMERICAL METHODS AND EXPERIMENTAL DATA

A. Extent of the $1/3$ and the $1/2$ plateaux

In Figure 9 we compare the numerical results of the phase boundaries of the $1/3$ plateau (a) and the $1/2$ plateau (b) as a function of J'/J , obtained with the various methods.

A good agreement between all the methods is found for the lower edge of the $1/3$ plateau in the whole parameter range $[0.5, 0.7]$ considered here. The series expansion results lie close to the iPEPS values. The $N = 36$ lattice used in ED (and DMRG) is compatible with the structure of the $1/3$ plateau state, but not with the $1/4$ plateau state. This explains why the $N = 36$ lattice overestimates the extent of the $1/3$ plateau on the lower edge for $J'/J \lesssim 0.65$, where we find a transition between the $1/4$ plateau and the $1/3$ plateau. For larger J'/J iPEPS predicts a transition between a $1/3$ supersolid phase and the $1/3$ plateau, i.e., structures which are both compatible with the $N = 36$ lattice, and therefore the agreement is better.

For the upper edge of the $1/3$ plateau a good agreement between iPEPS, and the $N = 36$ lattice from ED and DMRG can be found. This lattice is compatible with the structures of both adjacent phases, except for $J'/J \lesssim 0.55$ where iPEPS and SE predict a direct transition between the $1/3$ plateau and the $2/5$ plateau. The latter is not compatible with the $N = 36$ lattice and this is why the extent of the $1/3$ plateau is overestimated for $J'/J \lesssim 0.55$. We find a large deviation between SE and the other methods, which is difficult to explain. One possibility is that the phase transition is of second order with a very slow increase of the order parameter as a function of J'/J , which would be difficult to capture with the other methods. The low transition value found with DMRG on the 12×10 system also points towards this possibility. From iPEPS, however, we do not find indications for such a small order parameter over a wide range of J'/J . Nevertheless, such a scenario would still be compatible with the experimental data (and it could explain the slow increase of M/M_S in the $1/3$ plateau).

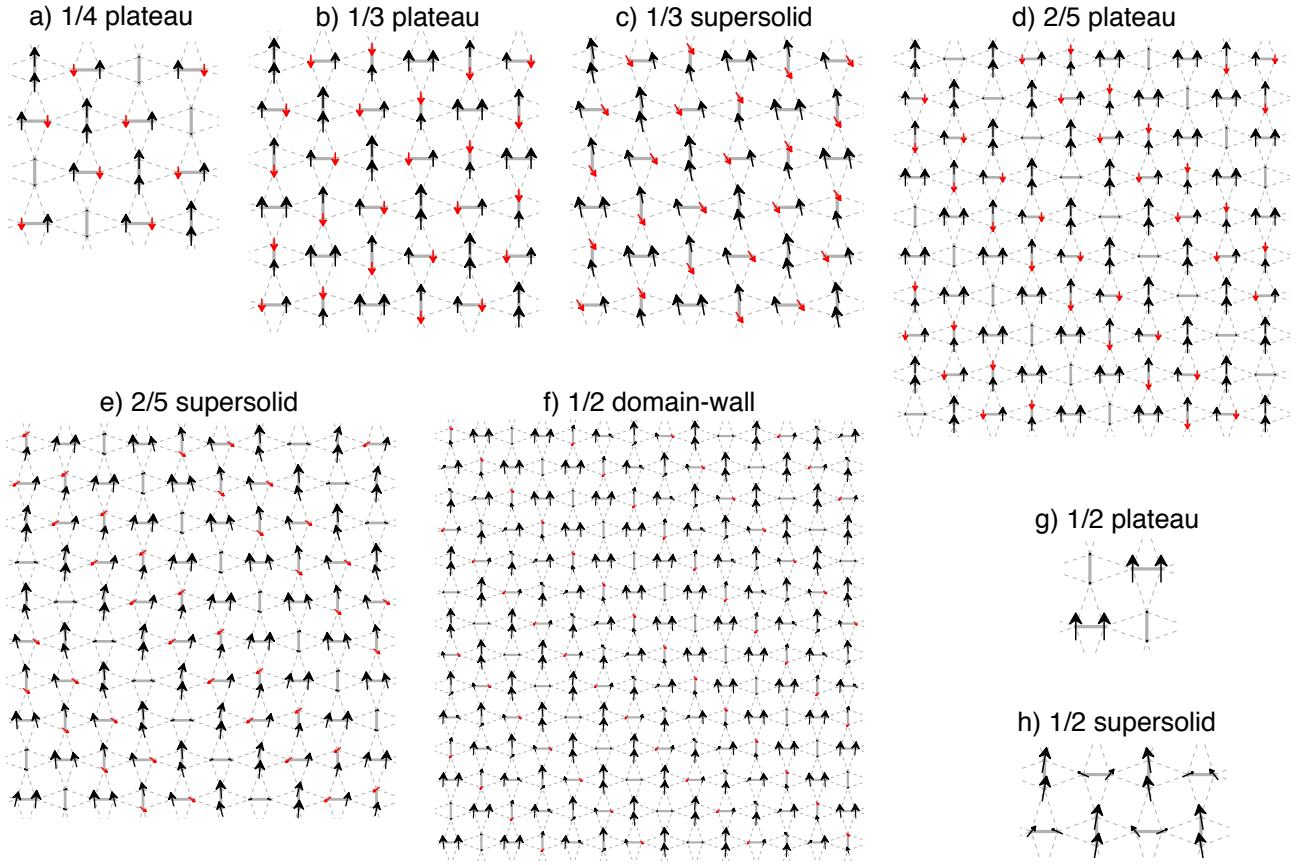


FIG. 8. Spin structure of the different phases obtained in different rectangular unit cells with iPEPS. The field direction is along the vertical axis, where the black spins predominantly point along the field, and the red spins predominantly point in the opposite direction of the field. The states in the plateaux have a vanishing transverse component, in contrast to the supersolid phases. Each supersolid state above a certain plateau is obtained by deforming (rotating) the spins of the state in the plateau. The 1/2 domain-wall phase contains stripes of the 1/2 plateau state, separated by (superfluid) domain walls.

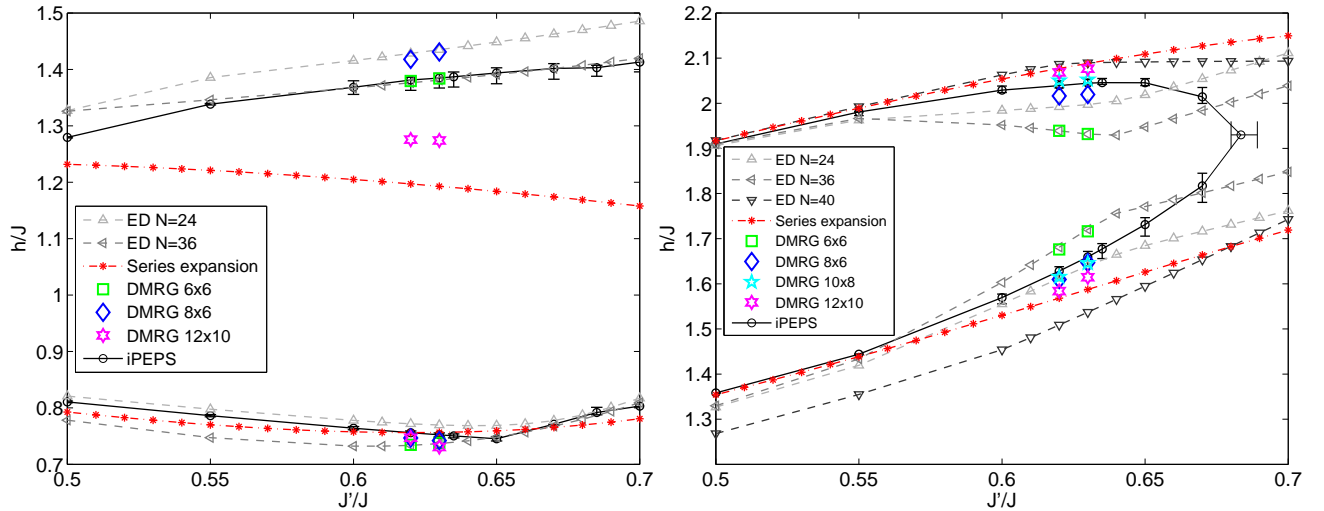


FIG. 9. Upper and lower boundary of the 1/3 plateau (a) and the 1/2 plateau (b) obtained with different methods.

In any case, the 1/3 plateau is rather wide in the parameter regime under consideration. This might be attributed to the

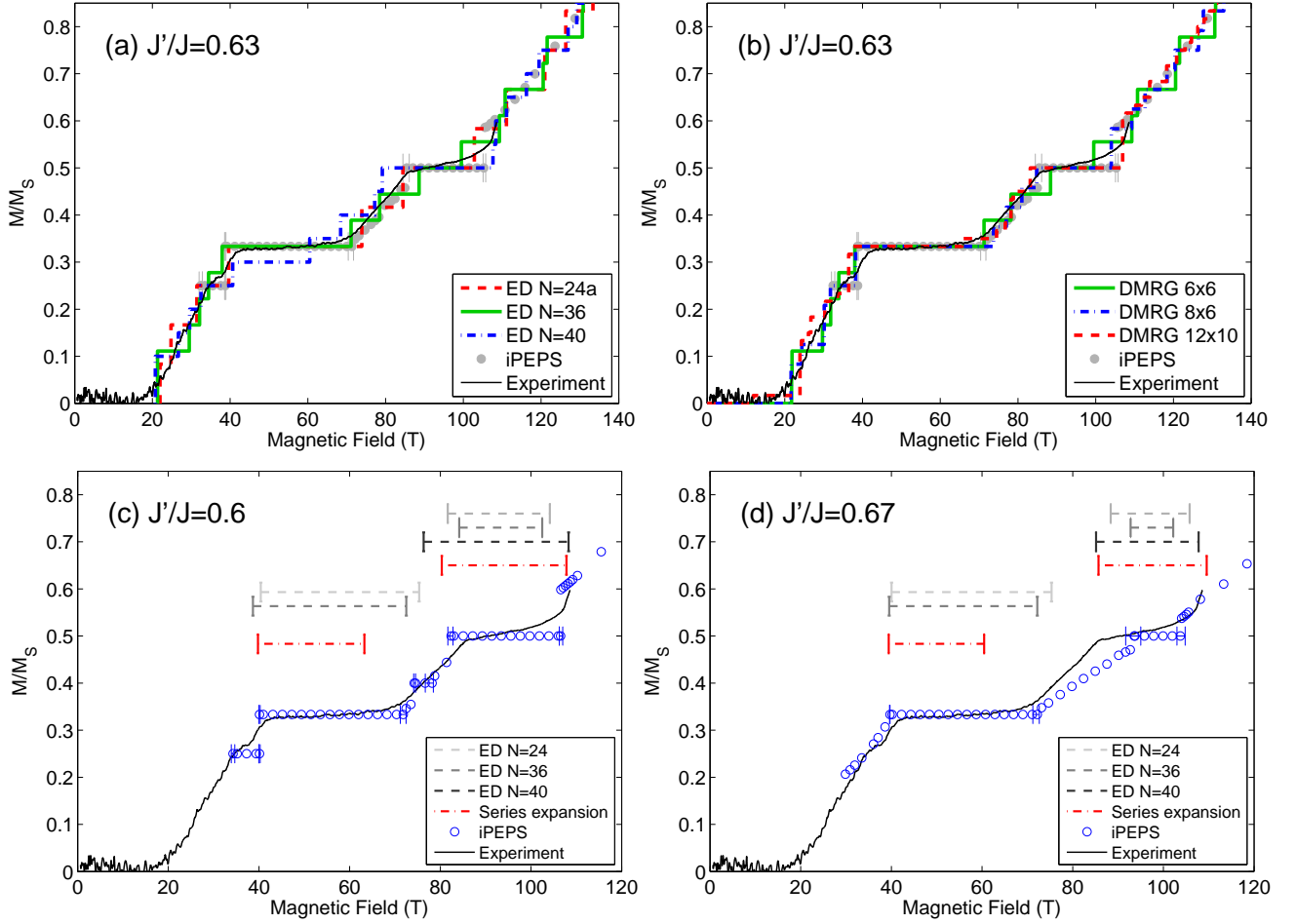


FIG. 10. Magnetization curves for $J'/J = 0.63$ obtained from experiments and iPEPS, compared to (a) ED, and (b) DMRG. (c-d) The experimental data is not compatible with the numerical magnetization curves for $J'/J = 0.6$ (c) and $J'/J = 0.67$ (d).

proximity to a classical plateau state at $J'/J = 1/2$ [28].

For the lower edge of the $1/2$ plateau we find a good agreement between iPEPS and SE for $J'/J \lesssim 0.55$, where both methods predict a direct transition between the $2/5$ plateau and the $1/2$ plateau. However, for $J'/J \gtrsim 0.55$ iPEPS predicts a supersolid (or domain-wall) phase adjacent to the $1/2$ plateau, which are not captured in the SE calculations, and this leads to an overestimation of the extent of the $1/2$ plateau with SE. There are rather large variations of the phase boundary for the different ED lattices. The iPEPS phase boundary lies in between the $N = 24$ lattice and the $N = 36$, $N = 40$ lattices (for $0.55 < J'/J < 0.65$).

Also for the upper edge of the $1/2$ plateau SE agrees with the iPEPS result for $J'/J \lesssim 0.55$, where both methods predict a transition between the $1/2$ plateau and the $1/2$ supersolid. For larger J'/J iPEPS finds a $1/3$ supersolid with a lower variational energy than the $1/2$ supersolid, which explains the deviation from the SE phase boundary. Large finite-size effects are found with ED also for the upper edge. The iPEPS result lies in between the $N = 24$, 36 and the $N = 40$ phase boundary for $J'/J < 0.65$. The $1/2$ plateau obtained with ED does not close in the considered parameter range due to finite-size effects.

Finally, the iPEPS results for the extent of the $1/2$ plateau are also compatible with the finite size DMRG data, where the best agreement is found with the 10×8 system.

B. Comparison of magnetization curves

In Fig. 10 we present a comparison of the magnetization curves between the different methods and the experiment.

Figure 10(a) shows a plot obtained with ED for different system sizes for $J'/J = 0.63$. Variations in the magnetization curves can be found for different lattice sizes, but there is an overall good agreement with iPEPS and the experimental data.

A good agreement is also found with DMRG as shown Fig. 10(b), although the finite-size effects on the upper edge of the $1/3$ plateau are rather large.

In Fig. 10(c) we present an attempted fit between iPEPS and experimental data for $J'/J = 0.6$, showing several mismatches. The $1/2$ plateau is considerably bigger than in the experimental data, and we clearly find a $2/5$ plateau at this value for $J'/J = 0.6$, which is absent in the experiment. We therefore conclude that $J'/J = 0.6$ is too small.

A bad fit is also obtained if J'/J is too large, as shown in Fig. 10(d) for $J'/J = 0.67$. The $1/2$ plateau turns out to be too small in this case, and the slope of the magnetization curve between the $1/3$ and $1/2$ plateau is not as steep as in the experiment.

-
- [1] M. Jaime, R. Daou, S. A. Crooker, F. Weickert, A. Uchida, A. E. Feiguin, C. D. Batista, H. A. Dabkowska, and B. D. Gaulin, *PNAS* **109**, 12404 (2012).
 - [2] S. Takeyama and E. Kojima, *J. Phys. D* **44**, 425003 (2011).
 - [3] A. Miyata, H. Ueda, Y. Ueda, H. Sawabe, and S. Takeyama, *Phys. Rev. Lett.* **107**, 207203 (2011).
 - [4] K. Nakao, F. Herlach, T. Goto, S. Takeyama, T. Sakakibara, and N. Miura, *J. Phys. E* **18**, 1018 (1985).
 - [5] N. Miura, T. Osada, and S. Takeyama, *J. Low Temp. Phys.* **133**, 139 (2003).
 - [6] S. Takeyama, R. Sakakura, Y. H. Matsuda, A. Miyata, and M. Tokunaga, *J. Phys. Soc. Jpn.* **81**, 014702 (2012).
 - [7] A. M. Läuchli, in *Introduction to Frustrated Magnetism*, Springer Series in Solid-State Sciences, Vol. 164, edited by C. Lacroix, P. Mendels, and F. Mila (Springer Berlin Heidelberg, 2011) pp. 481–511.
 - [8] J. Richter, J. Schulenburg, and A. Honecker, in *Quantum Magnetism*, Lecture Notes in Physics, Vol. 645, edited by U. Schollwöck, J. Richter, D. J. J. Farnell, and R. F. Bishop (Springer Berlin Heidelberg, 2004) pp. 85–153.
 - [9] A. Abendschein and S. Capponi, *Phys. Rev. Lett.* **101**, 227201 (2008).
 - [10] <http://www-e.uni-magdeburg.de/jschulen/spin/>.
 - [11] U. Schollwöck, *Rev. Mod. Phys.* **77**, 259 (2005).
 - [12] U. Schollwöck, *Annals of Physics* **326**, 96 (2011).
 - [13] E. Stoudenmire and S. R. White, *Annu. Rev. Condens. Matter Phys.* **3**, 111 (2012).
 - [14] S. Yan, D. A. Huse, and S. R. White, *Science* **332**, 1173 (2011).
 - [15] S. Depenbrock, I. P. McCulloch, and U. Schollwöck, *Phys. Rev. Lett.* **109**, 067201 (2012).
 - [16] H.-C. Jiang, Z. Wang, and L. Balents, *Nature Physics* **8**, 902 (2012).
 - [17] F. Verstraete and J. I. Cirac, Preprint (2004), [arXiv:cond-mat/0407066](https://arxiv.org/abs/cond-mat/0407066).
 - [18] J. Jordan, R. Orús, G. Vidal, F. Verstraete, and J. I. Cirac, *Phys. Rev. Lett.* **101**, 250602 (2008).
 - [19] P. Corboz, R. Orús, B. Bauer, and G. Vidal, *Phys. Rev. B* **81**, 165104 (2010).
 - [20] P. Corboz, S. R. White, G. Vidal, and M. Troyer, *Phys. Rev. B* **84**, 041108 (2011).
 - [21] P. Corboz and F. Mila, *Phys. Rev. B* **87**, 115144 (2013).
 - [22] B. Bauer, P. Corboz, R. Orús, and M. Troyer, *Phys. Rev. B* **83**, 125106 (2011).
 - [23] L. Messio, P. Corboz, and F. Mila, Preprint (2013), [arXiv:1304.7676](https://arxiv.org/abs/1304.7676).
 - [24] P.-O. Löwdin, *J. Math. Phys.* **3**, 969 (1962).
 - [25] M. Takahashi, *J. Phys. C* **10**, 1289 (1977).
 - [26] D. Klagges and K. P. Schmidt, *Phys. Rev. Lett.* **108**, 230508 (2012).
 - [27] We also have calculated the one-hole gap for $M = 1/2$ and $M = 1/3$ (removing one triplet t^1 from the plateau structure), but it plays no role for the magnetization curve of the Shastry-Sutherland model.
 - [28] M. Moliner, D. C. Cabra, A. Honecker, P. Pujol, and F. Stauffer, *Phys. Rev. B* **79**, 144401 (2009).